Water Reuse

Water Reuse Vol 13 No 2, 269 doi: 10.2166/wrd.2023.013

Economic analysis based on saline water treatment using renewable energy system and microgrid architecture

N. P. G. Bhavani[a], Kailash Harne[b], Satendar Singh[c], Ostonokulov Azamat Abdukarimovich[d], V. Balaji[e], Bharat Singh[f], K. Vengatesan[g] and Sachi Nandan Mohanty[h,*]

[a] Saveetha School of Engineering, SIMATS, Chennai, India
[b] Netaji Subhas University of Technology, New Delhi, Delhi, India
[c] Sharda University, Greater Noida, Uttar Pradesh, India
[d] Tashkent Institute of Finance, Tashkent, Uzbekistan
[e] Vardhaman College of Engineering, Hyderabad, India
[f] GLA University, Mathura, UP, India
[g] Sanjivani College of Engineering, Kopargaon, India
[h] Singidunum University, Belgrade, Serbia
*Corresponding author. E-mail: snandan.mohanty@singidunum.ac.rs

ABSTRACT

Reverse osmosis desalination facilities operating on microgrids (MGs) powered by renewable energy are becoming more significant. A leader-follower structured optimization method underlies the suggested algorithm. The desalination plant is divided into components, each of which can be operated separately as needed. MGs are becoming an important part of smart grids, which incorporate distributed renewable energy sources (RESs), energy storage devices, and load control strategies. This research proposes novel techniques in economic saline water treatment based on MG architecture integrated with a renewable energy systems. This study offers an optimization framework to simultaneously optimize saline as well as freshwater water sources, decentralized renewable and conventional energy sources to operate water-energy systems economically and efficiently. The radial Boltzmann basis machine is used to analyse the salinity of water. Data on water salinity were used to conduct the experimental analysis, which was evaluated for accuracy, precision, recall, and specificity as well as computational cost and kappa coefficient. The proposed method achieved 88% accuracy, 65% precision, 59% recall, 65% specificity, 59% computational cost, and 51% kappa coefficient.

Key words: economic analysis, microgrid architecture, renewable energy system, saline water treatment

HIGHLIGHTS

- Novel method in economic saline water treatment based on microgrid architecture integrated with a renewable energy system.
- An effective and cost-effective water-energy system can be operated by using an optimization framework that simultaneously improves salty and freshwater water sources as well as decentralized renewable and conventional energy sources.
- Salinity of water is analysed using a radial Boltzmann basis machine.

GRAPHICAL ABSTRACT

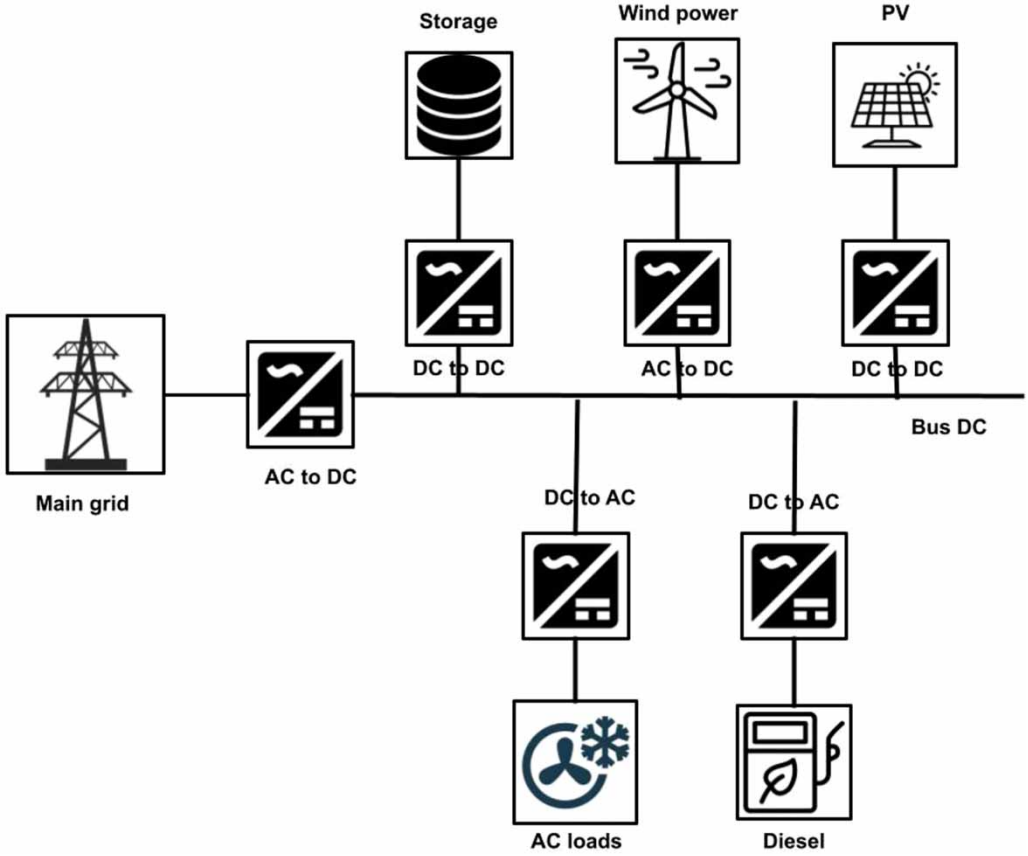

1. INTRODUCTION

The growing demand from other important industries like agriculture and manufacturing places additional emphasis on the availability of water for home use. Water use in the agricultural sector alone might increase by almost 19% by 2050 (Dokhani *et al.* 2022). The demand for water on a global scale is increasing by 1% annually and may reach 120–130% of the current demand in 2050. On the other hand, due to climatic change and other factors, freshwater sources are diminishing (Jabari *et al.* 2022). Freshwater generation appears to be a solution to the rising water demand. Desalination of plentiful seawater has become a viable technique for producing freshwater. Around 1% of the world's population currently receives water from desalination plants, and more plants are being built every year (Sui *et al.* 2021). Due to its reduced energy usage, which ranges from 3 to 6 kWh/m^3, reverse osmosis (RO) of membrane process is the most favoured approach for desalination. It should not come as a surprise that almost 60% of the desalination plants in the world employ RO technology. Reverse osmosis desalination (ROD) facilities have historically operated with traditional generators, which are polluting. Desalination utilizing renewable energy is becoming more and more important as environmental concerns resulting from pollution grow. The power generated by renewable sources is sporadic. To synchronize them, conventional generators and energy storage (ES) are typically also used. As a result, use of renewable energy resources (RERs) to generate electricity has increased. In comparison to conventional or traditional power sources, the power produced by RERs is thought to be more sustainable, affordable, and ecologically beneficial. When more than one renewable resource is included in generation mix, according to scientists who are working to integrate it into the network, there are various benefits, including a rise in power generation efficiency (Dong *et al.* 2022). As a result, it has been widely predicted that most nations' electricity will be produced by hybrid renewable energy integrated systems. This is also because a large portion of the current electricity system relies on environmentally harmful and rapidly diminishing fossil fuels (coal). When it comes to allowing for acceptable voltage variation and system frequency in any particular electrical network, integrating RERs poses a variety of issues. Currently, smart grid (SG)

technology offers a variety of approaches to address problems caused by the instability and fluctuation of RERs. Installation of a microgrid system (MG) is a crucial methodology that aids in the efficient usage of RERs. The goal of this strategy is to maximize system performance despite a variety of operational problems by establishing a peer-to-peer operation mode for electrical systems. Numerous RERs difficulties are thought to be resolved by energy storage systems (ESS). Energy storage acts as a dampening mechanism between energy demand and generation in the urban sector, where energy demand needs as well as RERs implementation issues are a concern (Hemmati *et al.* 2021).

The contribution of this research is as follows:

1. To propose a novel method in economic saline water treatment based on MG architecture integrated with a renewable energy system.
2. An effective and cost-effective water-energy system can be operated by using an optimization framework that simultaneously improves salty and freshwater water sources as well as decentralized renewable and conventional energy sources.
3. Salinity of water is analysed using a radial Boltzmann basis machine.

2. RELATED WORKS

The literature contains several water and energy co-optimization models where costs, energy use, or load demands of water systems were reduced (Prathapaneni & Detroja 2020). All models, however, did not account for desalination procedures and assumed that freshwater was the only supply of water. A desalination plant's ability to operate economically depends on energy reduction. The high electrical power requirements of desalination systems are one of their biggest obstacles. In Alzahrani *et al.* (2022), the economic and reliability concepts of the MGs are investigated. In He *et al.* (2022), the optimal placement of distributed generation (DG) resources is proposed, and suggested strategies are assessed. The increase in use of combined heat and power (CHP) DGs is also described in Vitale *et al.* (2021), in which it is objected to improving the reliability of MGs. The short-term generation scheduling for MGs is also evaluated in Wang *et al.* (2022). In Harish *et al.* (2022), a multi-objective optimization is conducted to deal with the energy management of MGs while the economic and environmental restrictions are taken into account. Several techniques, including physical models, machine learning (ML), and (more recently) deep learning (DL), can be used to forecast (Jalilian *et al.* 2022). They are used, for instance, to forecast and optimize energy use in smart MGs, anticipate energy use in the production of wheat, enhance health services, boost wireless network performance, manage floods, and forecast hydrogen production. Energy management of an MG made up of photovoltaic (PV), wind turbine (WT), and electrical storage system was resolved by the authors in Moazeni & Khazaei (2021) while satisfying the constraints of the MG. In Cruz *et al.* (2019), the uncertainty of solar, as well as wind power units, was taken into account when solving energy management of an MG. Latin hypercube sampling is utilized to manage uncertainty (Wu *et al.* 2021). The performance of failures in an MG was studied by Jumare (2020) and Okampo *et al.* (2022) under both dynamic and static loads, such as static power loads, static impedance loads, and current static loads. The major objective of this work was to investigate how the kind of load affected the fault performance of the independent MG using the WT as an energy resource. Mazzoni *et al.* (2019), Ogbonnaya *et al.* (2021), and Shayan *et al.* (2022) provided a thorough analysis of hybrid renewable MG optimization strategies.

3. SYSTEM MODEL

This section discusses novel methods in economic saline water treatment based on MG architecture integrated with renewable energy systems. To operate a water-energy system economically and efficiently, this study provides an optimization framework to simultaneously optimize salty and freshwater water sources as well as decentralized renewable and conventional energy sources. Utilizing a deep radial Boltzmann basis machine, salinity of water is examined. ES devices, loads, and distributed power sources typically make up MG. More and more deep row entrenchment (DRE) will be adopted as renewable energy technology advances. One of the efficient approaches to DRE linked to the electrical grid is MG.

Figure 1 depicts an example of a typical renewable energy-based MG. Through ES-based energy management, MG was able to efficiently coordinate DRE and the power grid (PG) and minimize drawbacks brought on by high penetration of DRE in PG. DRE is becoming more and more integrated into the electrical grid. The management and operation of the grid are greatly hampered by intermittent power outputs of DRE. The electricity distribution network, distributed renewable energy systems, and ESS may all be easily separated to form the smart grid. In Figure 1, a typical construction is shown.

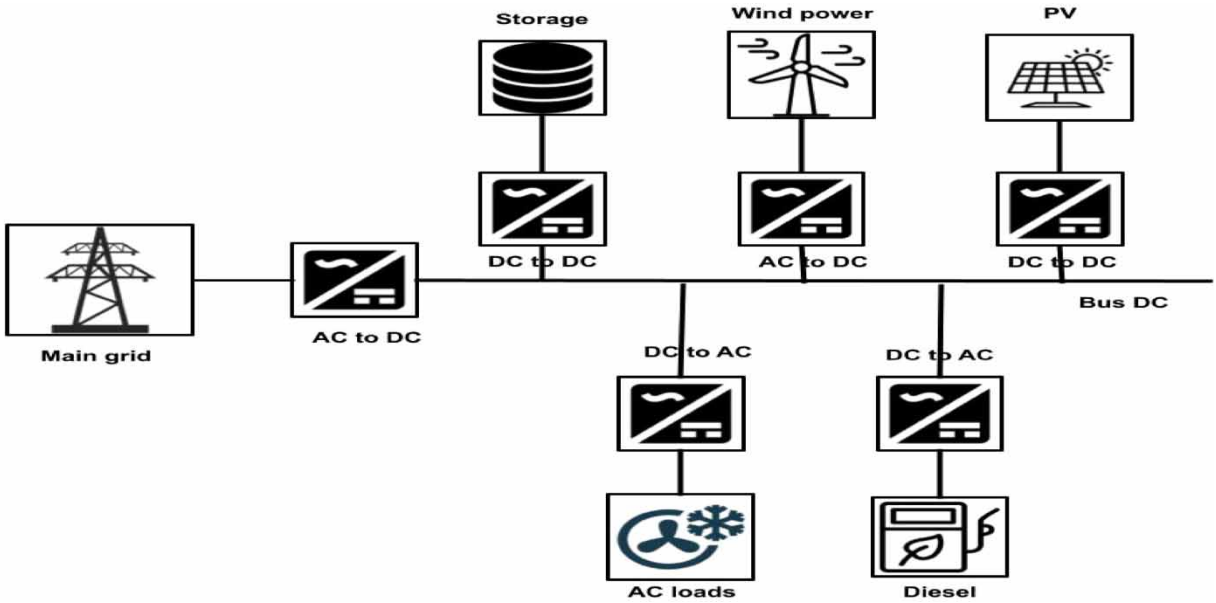

Figure 1 | Microgrid structure.

The primary components of the power grid, as depicted in Figure 2, are electric wires, transformers, and electrical loads. The smart grid also incorporates some dispersed generation technologies, such as solar and wind energy sources. ESS, which performs the roles of both a supply device and a storage device, is connected to the power distribution system in the meantime. The energy storage technology improves electric power distribution flexibility and lowers power generation loss. The grid system is also a radial one, with many batteries connected to users, mostly electric vehicles and hot water tanks. When some areas are experiencing problems, the smart grids can obtain some rescued electricity with the use of ESS. The ESS is created and integrated into one component for storing and supplying electricity, which simplifies the topic on which we are focused. If we assume that one bus has a defect, the concurrent downstream area that is not faulty will also go dark. The faulty bus can be saved by its related storage system on the one hand with the aid of a storage system. The system's topological structure does not change. On the other side, if its related storage system is unable to continue the assistance, the malfunctioning bus will signal other buses to 'rescue' it. As a result, the system's topological structure needs to be modified. The restoration technique causes the underpowered load to be transferred to other buses, changing the topological structure of the system and creating a load imbalance. With load balancing acting as a restriction, the goal

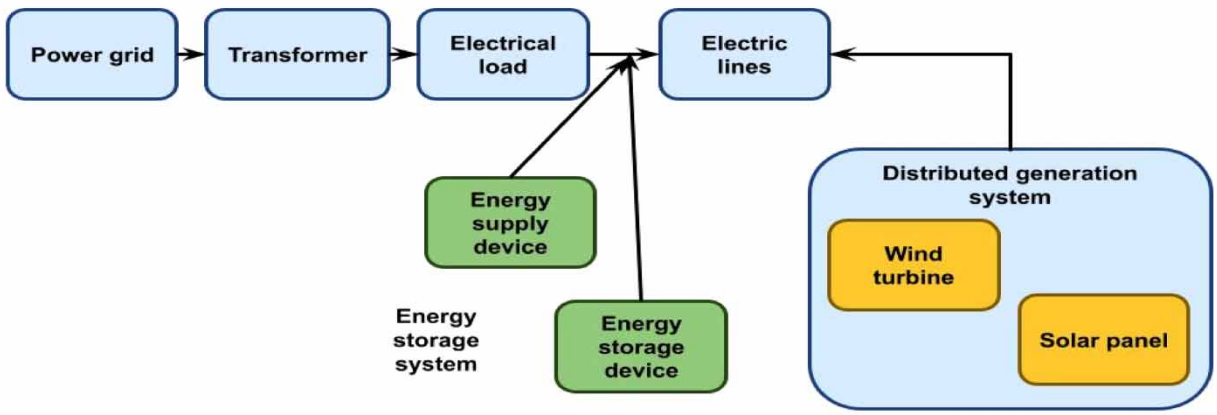

Figure 2 | Structure of a power grid.

of this article is to increase the system's reliability during the restoration process. The P-N junction of semiconductors exhibits PV effect. The PV cell model that is being developed in this work is based on static operation of a typical P-N junction diode. This model is made up of a diode D, a shunt resistor R_p, a series resistor R_s, and a direct current source I_{ph} connected in parallel. The necessary voltages and currents are supplied by applying a series–parallel combination of suitable solar panels and cells. Equation (1) is used to determine the cell output current I_{PVc}:

$$I_{PVc} = I_{ph} - I_{Dc} - I_{Rpc} = I_{ph} - I_o \cdot \left[\exp\left(q \cdot \frac{V_{PVc} + R_s I_{PVc}}{AKT}\right) - 1\right] - \frac{V_{PVc} + R_s I_{PVc}}{R_p} \tag{1}$$

where K is Boltzmann's constant, and T is the temperature of PV cell. According to Equation (2), the current I_{ph} is linearly related to PV cell temperature T and inversely proportional to the sun irradiation G_r value:

$$I_{ph} = [I_{sc} + K_i \cdot (T - 298)] \cdot G_r/1,000 \tag{2}$$

where G_r is solar irradiation (W/m^2); I_{sc} is the PV cell's short-circuit current; K_i is the temperature coefficient of the short-circuit current (A/K); Array is made up of a series of parallel connections between the PV cells. The PV array's output current, I_{PV}, can be stated in the form of Equation (3):

$$I_{PV} = N_p \cdot I_{ph} - N_p \cdot I_o \left(\exp\left(q \cdot \frac{V_{PV} + \frac{N_s}{N_p} R_s I_{PV}}{N_s N_p AKT}\right) - 1\right) - \frac{V_{PV} + \frac{N_s}{N_p} R_s I_{PV}}{\frac{N_s}{N_p} R_p} \tag{3}$$

The following equation can be used to explain electrical power P_{PV} of the PV array:

$$P_{PV} = I_{PV} \cdot V_{PV} \tag{4}$$

A nonlinear function of operating voltage can be used to express the power of a PV array; this function has massively parallel processing (MPP). These characteristics indicate that PV array's voltage and power are falling as irradiation levels are dropping. The difference between the PV cell's absorbed photon flux and radiative photon flux in radiative recombination by Equation (5) determines net number of photons absorbed per unit area, which in turn determines current density J_{PV} in PV cell.

$$\frac{J_{PV}}{e} = \frac{A_{Con}}{A_{PV}} \int_{\varepsilon_{gPV}}^{\varepsilon_{max}} \frac{S_{AM.5}}{\varepsilon} d\varepsilon - \frac{2\pi}{h^3 c^2} \int_{\varepsilon_{gPV}}^{\varepsilon_{max}} \frac{\varepsilon^2 d\varepsilon}{\exp[(\varepsilon - eV_{PV})/(k_B T_{PV})] - 1} \tag{5}$$

The power output of PV cell is calculated using Equations (5) and (6):

$$P_{PV} = q_1 - q_{Cr} - q_{PVl} = J_{PV} A_{PV} V_{PV} \tag{6}$$

and efficiency is given by Equation (7):

$$\eta'_{PV} = \frac{P_{PV}}{q_1} \tag{7}$$

$$\grave{N}(\varepsilon_1, \varepsilon_2, T_E, \mu) = \frac{2\pi}{h^3 c^2} \int_{\varepsilon_1}^{\varepsilon_2} \frac{\varepsilon^2 d\varepsilon}{\exp[(\varepsilon - \mu)/(k_B T_E)] - 1} \tag{8}$$

and

$$\grave{E}(\varepsilon_1, \varepsilon_2, T_E, \mu) = \frac{2\pi}{h^3 c^2} \int_{\varepsilon_1}^{\varepsilon_2} \frac{\varepsilon^3 d\varepsilon}{\exp[(\varepsilon - \mu)/(k_B T_E)] - 1} \tag{9}$$

The radiation of photovoltaic cell (TPV) cell's current density can be expressed as Equation (10):

$$\frac{J_{\mathrm{TPV}}}{e} = f_{\mathrm{EC}}\dot{N}\left(\varepsilon_{\mathrm{gTPV}}, \infty, T_{\mathrm{E}}, 0\right) - (1 - f_{\mathrm{CC}})\dot{N}\left(\varepsilon_{\mathrm{gTPV}}, \infty, T_{\mathrm{TPV}}, eV_{\mathrm{TPV}}\right) - \chi^2(1 - \gamma_{\mathrm{BR}})\dot{N}\left(\varepsilon_{\mathrm{gTPV}}, \infty, T_{\mathrm{TPV}}, eV_{\mathrm{TPV}}\right) \tag{10}$$

where V_{TPV} is the TPV cell's output voltage, c is the cell's refractive index, g_{BR} is reflectivity of backside reflector, f_{EC} is view factor between emitter and TPV cell, f_{CC} is view factor between cells, and emitter cut-off energy is typically taken to be zero. The general flow of plug-in hybrid electric vehicles (PHEVs) is shown in Figure 3, which includes a charging unit, battery, UC bank, a shared DC bus, and a load. A DC–DC buck converter and an unregulated bridge rectifier are connected to the main supply to enhance the charge of battery being charged by the charger.

Low level control: Power converters must be controlled to regulate DC bus and allow localised current to flow in both directions.

High level control: Method is designed to monitor the SoC (state of charge) and guarantee complete PHEV stability.

Every MG consists of several distributed energy resources, each of which has a local controller. These controllers keep an eye on the MG's real power, reactive power, and frequency and distribute power across the VSC-HVDC link properly to maintain the stability of the entire system. Figure 4 shows architecture of the distributed control scheme. In an MG, controllers interact with one another and adjust power flow through VSC-HVDC to meet demand if active or reactive power generation and demand are out of sync. The communication network shown in Figure 4 is used to share mismatches of active power ($Pi = P_{\mathrm{gi}}\ P_{\mathrm{di}}$), reactive power ($Qi = Q_{\mathrm{gi}}\ P_{\mathrm{di}}$), and frequencies

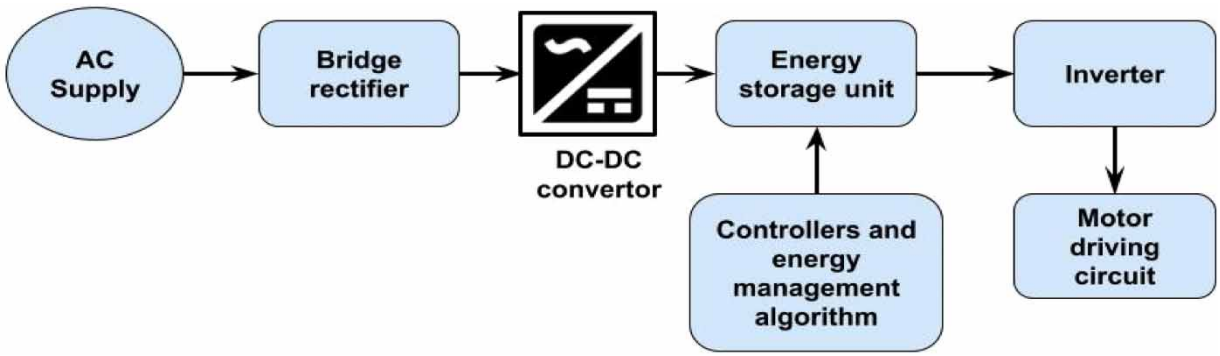

Figure 3 | General block diagram of PHEV.

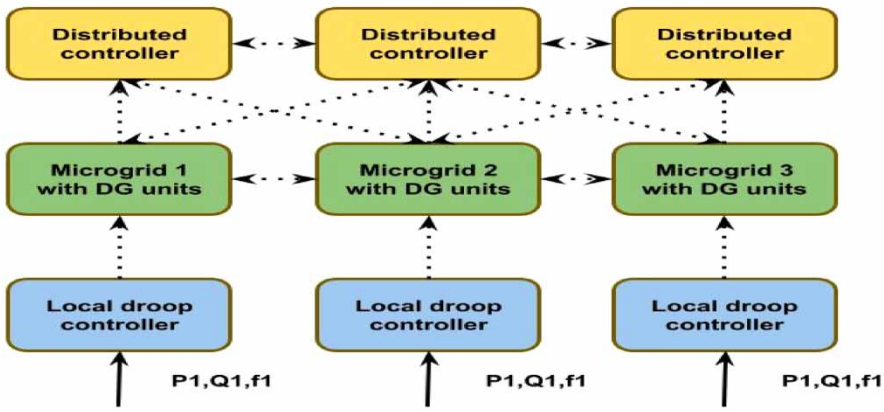

Figure 4 | Architecture of the distributed control scheme.

($fi = 50$ *fi*) between MGs and distributed controllers. When compared to centralised control, which transmits information over a great distance, the communication network is easier to use and more dependable for exchanging information among nearby subsystems. Digital communication networks provide intersystem communication, resulting in greater control design flexibility because surrounding subsystem states can be used for distributed control instead of only local subsystem information.

The bidirectional converter balances load output and consumption while maintaining a fixed voltage of 300 V.

Deep radial Boltzmann basis machine-based saline water analysis:

Equation (11) can be used to represent the broad fuzzy regression model:

$$Y = f(X)\{+\}\epsilon \tag{11}$$

The saline water analysis based on radial basis fuzzy system (SRBFS) layer can linearly receive input signal vector $X(t)$. It was believed that exponential sigmoid with fuzzy membership would make up the radial basis kernel function. After that, Equation (12) returns the output of the jth SRBFS:

$$h_j(X(t)) = \frac{1}{1+\exp\left(-a\left(-d_v^2\left(X(t),\dot{Z}_j(t)\right)/\sigma^2\right)-c\right)} \tag{12}$$

$Z_j(t)$ is kernel centre vector in jth Fuzzy radial basis network (FRBN). Morphological parameters a and c. The output of an FRBNN is a fuzzy linear weighted sum of outputs from hidden layer nodes. It is calculable using Equation (13):

$$\dot{y} = F(\dot{X}(t)) = \sum_{j=1}^{m} \dot{w}_j \cdot h_j(\dot{X}(t)) \tag{13}$$

Energy functions as well as maximum probability assumptions are included in modelling. The learning objective of RBMs, which are energy-based methods, is maximum likelihood. Energy of its hidden variables h and visible variables v in joint configuration is given by Equation (14):

$$E(\mathbf{v}, \mathbf{h}; \theta) = -\sum_{ij} \mathbf{W}_{ij}\mathbf{v}_i\mathbf{h}_j - \sum_i \mathbf{b}_i\mathbf{v}_i - \sum_i \mathbf{a}_j\mathbf{h}_j \tag{14}$$

θ stands for the variable $W(a,b)$. It is possible to determine the joint probability of v and h by Equation (15):

$$P_\theta(\mathbf{v}, \mathbf{h}) = \frac{1}{Z(\theta)}\exp(-E(\mathbf{v}, \mathbf{h}; \theta)) \tag{15}$$

The partition function in this context is denoted by $Z(\theta)$. The preceding equation can alternatively be expressed as Equation (16):

$$P_\theta(\mathbf{v}, \mathbf{h}) = \frac{1}{Z(\theta)}\exp\left(\sum_{i=1}^{D}\sum_{j=1}^{F}\mathbf{W}_{ij}\mathbf{v}_i\mathbf{h}_j + \sum_{i=1}^{D}\mathbf{v}_i\mathbf{b}_i + \sum_{j=1}^{F}\mathbf{h}_j\mathbf{a}_j\right) \tag{16}$$

Maximizing the likelihood function P is the goal (v). The edge distribution of $P(v, h)$ allows for the calculation of $P(v)$ by Equation (17):

$$P_\theta(\mathbf{v}) = \frac{1}{Z(\theta)}\sum_{\mathbf{h}}\exp[\mathbf{v}^T\mathbf{W}\mathbf{h} + \mathbf{a}^T\mathbf{h} + \mathbf{b}^T\mathbf{v}] \tag{17}$$

The RBM parameters are obtained by maximizing $P(v)$. We maximize $\log(P(v)) = L(\theta)$ to maximize $P(v)$ by Equation (18):

$$L(\theta) = \frac{1}{N}\sum_{n=1}^{N}\log P_\theta(\mathbf{v}^{(n)}) \tag{18}$$

First, stochastic gradient descent is used to maximize $L(\theta)$. The $L(\theta)$ derivative for W is then calculated as Equation (19):

$$\frac{\partial L(\theta)}{\partial \mathbf{W}_{ij}} = \frac{1}{N}\sum_{n=1}^{N}\frac{\partial}{\partial W_{ij}}\log\left(\sum_{\mathbf{h}}\exp[\mathbf{v}^{(n)T}\mathbf{W}\mathbf{h} + \mathbf{a}^T\mathbf{h} + \mathbf{b}^T\mathbf{v}^{(n)}]\right) - \frac{\partial}{\partial W_{ij}}\log Z(\theta) = E_{P_{\text{dut}}}[\mathbf{v}_i\mathbf{h}_j] - E_{P_\theta}[\mathbf{v}_i\mathbf{h}_j] \tag{19}$$

The first half of the formula is easy to evaluate. The average v_i and h_j values across all datasets are evaluated. The second half of the equation, which contains all $2|v| + |h|$ combinations of v and h, is difficult to solve due to its computational complexity. Equation (20) represents the second part of the formula:

$$\sum_{v,h}\mathbf{v}_i\mathbf{h}_j P_\theta(\mathbf{v}, \mathbf{h}) \tag{20}$$

Because it is not possible to compute analytical solution of gradient, available training strategies are mostly based on sampling techniques. Gradient is then substantially approximated using Equation (21) using Monte Carlo simulations:

$$\begin{aligned}
\Delta\mathbf{a}_i &= v_i^{(0)} - v_i^{(k)} \\
\Delta\mathbf{b}_i &= P(\mathbf{h}_j = 1|\mathbf{v}^{(0)}) - P(\mathbf{h}_j = 1|\mathbf{v}^{(k)}) \\
\Delta\mathbf{W}_{ij} &= P(\mathbf{h}_j = 1|\mathbf{v}^{(0)})\mathbf{v}_i^{(0)} - P(\mathbf{h}_j = 1|\mathbf{v}^{(k)})\mathbf{v}_i^{(k)}
\end{aligned} \tag{21}$$

Finally, Equation (22) offers an equation for the parameter update:

$$\mathbf{a}_i = \mathbf{a}_i + \Delta\mathrm{a}_i\mathbf{b}_j = \mathbf{b}_j + \Delta\mathbf{b}_j\mathbf{W}_{ij} = \mathbf{W}_{ij} + \Delta\mathbf{W}_{ij} \tag{22}$$

In the deep belief model (DBM) with one visible layer and two hidden layers, $h(1)$ and h, have a look at joint probability distribution of energy function E.

4. PERFORMANCE ANALYSIS

The machine used for the experiment has the following hardware components: an Intel Core i5 7200U processor, 8 GB of RAM, a 1 TB hard drive, and NVIDIA GTX 760MX graphics. Additionally, Python 3.5 environments were used to simulate how the suggested strategy might be put into practise. To establish the results of the offered technique, we carried out a statistical analysis by evaluating expected performance.

Dataset description: Datasets included following variables: feed flow rate ($F = 400$–600 L/h), permeate flux (P_{flux} (L/h m^2)), condenser inlet temperature ($T_{\text{cond}} = 20$–30 °C), evaporator inlet temperature ($T_{\text{evap}} = 60$–80 °C), and feed salt content ($S = 35$–140 g/L). Permeate flux was the main output. Data has also been divided into three categories for

Table 1 | Analysis based on water salinity composition

Dataset	Techniques	Accuracy	Precision	Recall	Specificity	Computational cost	Kappa coefficient
$S = 35$–140 g/L	CHP	77	55	42	51	45	41
	ML	79	59	43	53	48	43
	EA_SWT_MGA	81	61	45	55	51	45
$T_{\text{cond}} = 20$–30 °C	CHP	79	59	48	55	48	43
	ML	83	63	49	59	53	45
	EA_SWT_MGA	85	65	52	61	55	48
$T_{\text{evap}} = 60$–80 °C	CHP	82	62	53	59	52	45
	ML	85	63	55	63	55	49
	EA_SWT_MGA	88	65	59	65	59	51

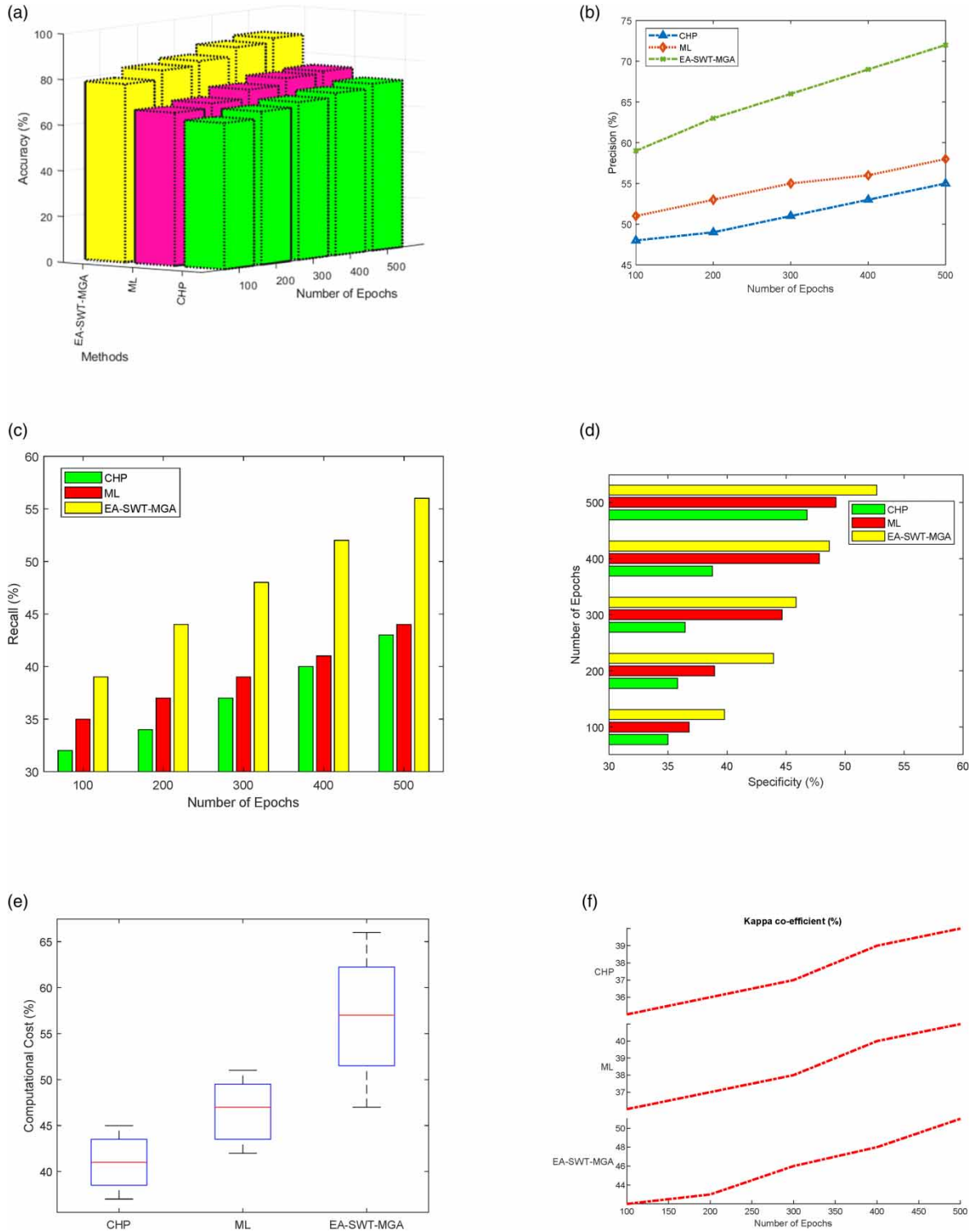

Figure 5 | Analysis for $S = 35–140$ g/L. (a) Accuracy, (b) Precision, (c) Recall, (d) Specificity, (e) Computational cost, (f) Kappa coefficient.

training, validation, and testing to facilitate neural network (NN) training. Model parameters are normally obtained from the training division. Validation division verifies accuracy of continuous training while testing division verifies its performance to avoid overfitting.

Table 1 shows analysis based on water salinity composition. The salinity ranges analysed are $S = 35–140$ g/L, $T_{cond} = 20–30$ °C, $T_{evap} = 60–80$ °C in terms of accuracy, precision, recall, and specificity, computational cost, and kappa coefficient.

Figure 5(a)–5(f) shows analysis for $S = 35–140$ g/L. The proposed technique attained accuracy 81%, precision 61%, recall 45%, specificity 55%, computational cost 51%, and kappa coefficient 45%; CHP attained accuracy 77%, precision 55%, recall 42%, specificity of 51%, computational cost 45%, and kappa coefficient 41%; ML attained accuracy 79%, precision 59%, recall 43%, specificity 53%, computational cost 48%, and kappa coefficient 43%.

Figure 6(a)–6(f) analysis has been shown for $T_{cond} = 20–30$ °C. The proposed technique attained accuracy 85%, precision 65%, recall 52%, specificity 61%, computational cost 55%, and kappa coefficient 48%; CHP attained accuracy 79%, precision

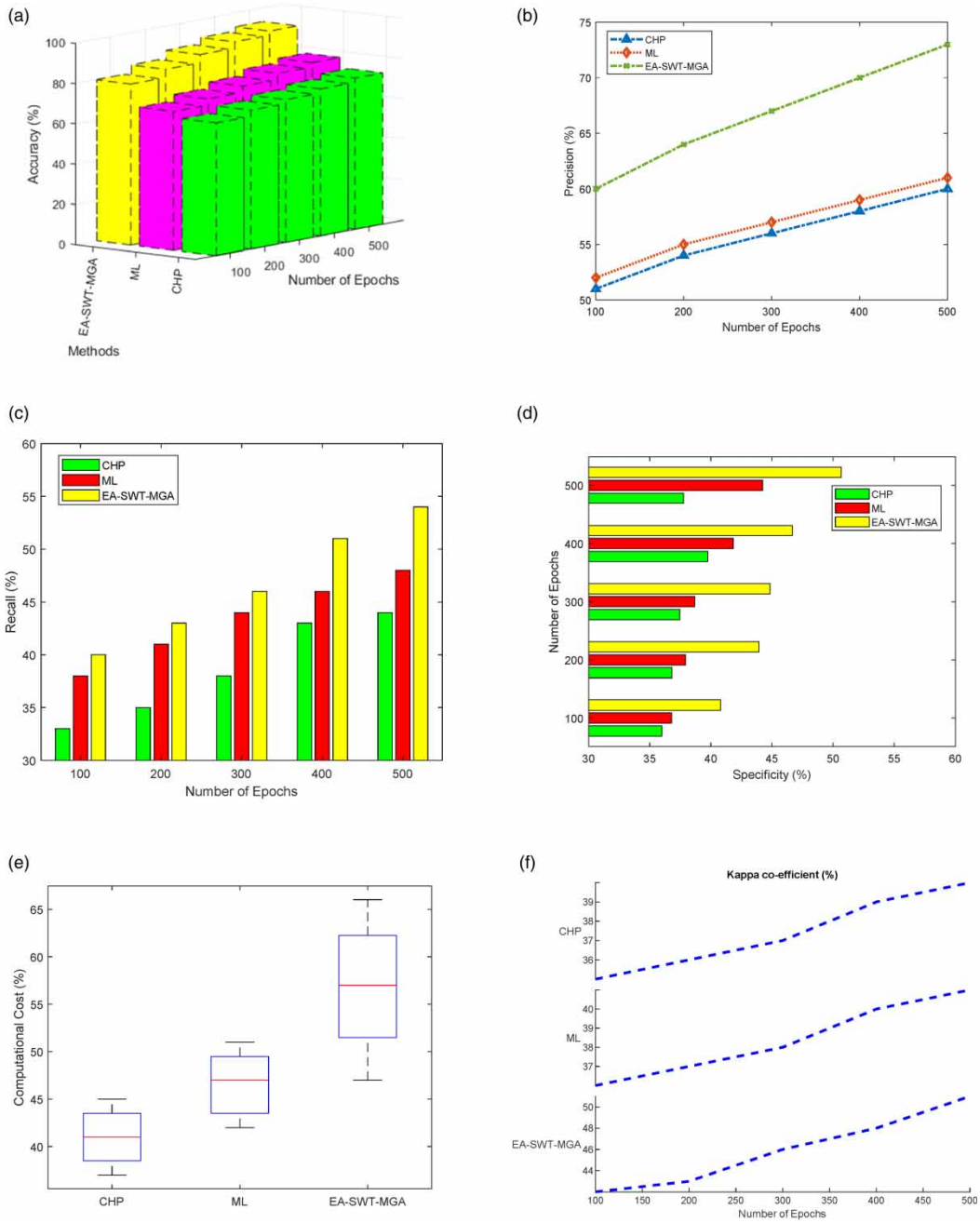

Figure 6 | Analysis for $T_{cond} = 20–30$ °C. (a) Accuracy, (b) Precision, (c) Recall, (d) Specificity, (e) Computational cost, (f) Kappa coefficient.

59%, recall 48%, specificity 55%, computational cost 48%, and kappa coefficient 43%; ML attained accuracy 83%, precision 63%, recall 49%, specificity 59%, computational cost 53%, and kappa coefficient 45%.

Figure 7(a)–7(f) shows analysis for $T_{evap} = 60$–80 °C. The proposed technique attained accuracy 88%, precision 65%, recall 59%, specificity 65%, computational cost 59%, and kappa coefficient 51%; CHP attained accuracy 82%, precision 62%, recall 53%, specificity 59%, computational cost 52%, and kappa coefficient 45%; ML attained accuracy 85%, precision 63%, recall 55%, specificity 63%, computational cost 55%, and kappa coefficient 49%.

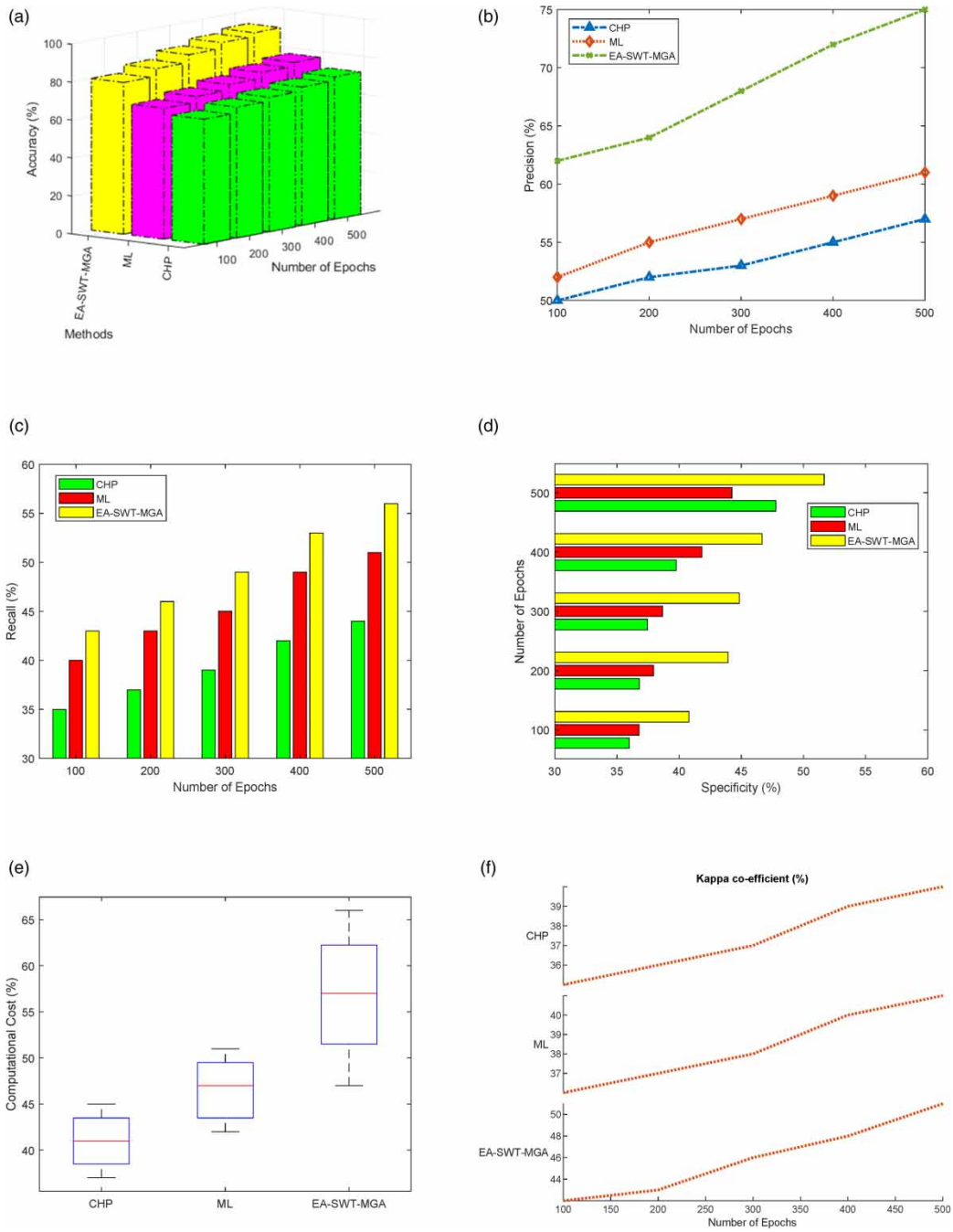

Figure 7 | (a)–(f) analysis for $T_{evap} = 60$–80 °C. (a) Accuracy, (b) Precision, (c) Recall, (d) Specificity, (e) Computational cost, (f) Kappa coefficient.

5. CONCLUSION

This research proposes a novel technique in economic saline water treatment based on MG architecture integrated with a renewable energy system. The salinity of water is analysed using a radial Boltzmann basis machine. To ease hydraulic coupling restrictions and guarantee the security of the water supply, a novel supply model that assesses the dependency between the major water saline supply (WSS) and various islanded subsystems, hydraulic stability, and desalination characteristics are constructed. When examining the location of the case, low-cost power-generating options were evaluated using renewable resources such as PV devices, wind turbines, and electricity from the grid. The proposed method achieved 88% accuracy, 65% precision, 59% recall, 65% specificity, 59% computational cost, and 51% kappa coefficient.

DATA AVAILABILITY STATEMENT

All relevant data are included in the paper or its Supplementary Information.

CONFLICT OF INTEREST

The authors declare there is no conflict.

REFERENCES

Alzahrani, A., Ramu, S. K., Devarajan, G., Vairavasundaram, I. & Vairavasundaram, S. 2022 A review on hydrogen-based hybrid microgrid system: topologies for hydrogen energy storage, integration, and energy management with solar and wind energy. *Energies* **15** (21), 7979.

Cruz, H., Law, Y. Y., Guest, J. S., Rabaey, K., Batstone, D., Laycock, B., Verstraete, W. & Pikaar, I. 2019 Mainstream ammonium recovery to advance sustainable urban wastewater management. *Environmental Science & Technology* **53** (19), 11066–11079.

Dokhani, S., Assadi, M. & Pollet, B. G. 2022 Techno-economic assessment of hydrogen production from seawater. *International Journal of Hydrogen Energy* **48** (26), 9592–9608.

Dong, Y., Liu, F., Lu, X., Lou, Y., Ma, Y. & Eghbalian, N. 2022 Multi-objective economic environmental energy management microgrid using hybrid energy storage implementing and developed Manta Ray Foraging Optimization Algorithm. *Electric Power Systems Research* **211**, 108181.

Harish, V. S. K. V., Anwer, N. & Kumar, A. 2022 Applications, planning and socio-techno-economic analysis of distributed energy systems for rural electrification in India and other countries: A review. *Sustainable Energy Technologies and Assessments* **52**, 102032.

He, Y., Guo, S., Dong, P., Wang, C., Huang, J. & Zhou, J. 2022 Techno-economic comparison of different hybrid energy storage systems for off-grid renewable energy applications based on a novel probabilistic reliability index. *Applied Energy* **328**, 120225.

Hemmati, M., Mirzaei, M. A., Abapour, M., Zare, K., Mohammadi-ivatloo, B., Mehrjerdi, H. & Marzband, M. 2021 Economic-environmental analysis of combined heat and power-based reconfigurable microgrid integrated with multiple energy storage and demand response program. *Sustainable Cities and Society* **69**, 102790.

Jabari, F., Arasteh, H., Sheikhi-Fini, A., Ghaebi, H., Bannae-Sharifian, M. B., Mohammadi-Ivatloo, B. & Mohammadpourfard, M. 2022 A biogas-steam combined cycle for sustainable development of industrial-scale water-power hybrid microgrids: Design and optimal scheduling. *Biofuels, Bioproducts and Biorefining* **16** (1), 172–192.

Jalilian, F., Mirzaei, M. A., Zare, K., Mohammadi-Ivatloo, B., Marzband, M. & Anvari-Moghaddam, A. 2022 Multi-energy microgrids: an optimal despatch model for water-energy nexus. *Sustainable Cities and Society* **77**, 103573.

Jumare, I. A. 2020 Energy storage with salt water battery: A preliminary design and economic assessment. *Journal of Energy Storage* **27**, 101130.

Mazzoni, S., Ooi, S., Nastasi, B. & Romagnoli, A. 2019 Energy storage technologies as techno-economic parameters for master-planning and optimal dispatch in smart multi energy systems. *Applied Energy* **254**, 113682.

Moazeni, F. & Khazaei, J. 2021 Optimal design and operation of an islanded water-energy network including a combined electrodialysis-reverse osmosis desalination unit. *Renewable Energy* **167**, 395–408.

Ogbonnaya, C., Abeykoon, C., Nasser, A., Turan, A. & Ume, C. S. 2021 Prospects of integrated photovoltaic-fuel cell systems in a hydrogen economy: A comprehensive review. *Energies* **14** (20), 6827.

Okampo, E. J., Nwulu, N. & Bokoro, P. N. 2022 Economic and reliability assessment of hybrid PRO-RO desalination systems using brine for salinity gradient energy production. *Sustainability* **14** (6), 3328.

Prathapaneni, D. R. & Detroja, K. 2020 Optimal design of energy sources and reverse osmosis desalination plant with demand side management for cost-effective freshwater production. *Desalination* **496**, 114741.

Shayan, M. E., Najafi, G., Ghobadian, B., Gorjian, S., Mamat, R. & Ghazali, M. F. 2022 Multi-microgrid optimization and energy management under boost voltage converter with Markov prediction chain and dynamic decision algorithm. *Renewable Energy* **201**, 179–189.

Sui, Q., Wei, F., Lin, X. & Li, Z. 2021 Optimal energy management of a renewable microgrid integrating water supply systems. *International Journal of Electrical Power & Energy Systems* **125**, 106445.

Vitale, F., Rispoli, N., Sorrentino, M., Rosen, M. A. & Pianese, C. 2021 On the use of dynamic programming for optimal energy management of grid-connected reversible solid oxide cell-based renewable microgrids. *Energy* **225**, 120304.

Wang, W., Wang, D., Zhao, Y., Yu, Y. & Wang, Y. 2022 Research on capacity optimization and real-time control of island microgrid considering time-shifting load. *Energy Reports* **8**, 990–997.

Wu, Y., Hu, M., Liao, M., Liu, F. & Xu, C. 2021 Risk assessment of renewable energy-based island microgrid using the HFLTS-cloud model method. *Journal of Cleaner Production* **284**, 125362.

First received 9 February 2023; accepted in revised form 12 April 2023. Available online 17 May 2023